Bioactive Materials 12 (2022) 30–41

Contents lists available at ScienceDirect

Bioactive Materials

journal homepage: www.keaipublishing.com/en/journals/bioactive-materials

Effect of silver in thermal treatments of Fe-Mn-C degradable metals: Implications for stent processing

Sergio Loffredo [a,b], Sofia Gambaro [a,c], Francesco Copes [a], Carlo Paternoster [a], Nicolas Giguère [d], Maurizio Vedani [b], Diego Mantovani [a,*]

[a] Laboratory for Biomaterials and Bioengineering, Canada Research Chair I in Biomaterials and Bioengineering for the Innovation in Surgery, Department of Min-Met-Materials Engineering, Research Center of CHU de Quebec, Division of Regenerative Medicine, Laval University, Quebec City, QC G1V 0A6, Canada
[b] Department of Mechanical Engineering, Politecnico di Milano, Milan, 20156, Italy
[c] National Research Council, Institute of Condensed Matter Chemistry and Technologies for Energy CNR-ICMATE, Genoa, 16149, Italy
[d] Quebec Metallurgy Center CMQ, Trois-Rivières, QC, G9A 5E1, Canada

ARTICLE INFO

Keywords:
Twinning
Recrystallization
Biomaterials
Silver
Steels

ABSTRACT

Twinning-induced plasticity (TWIP) steels are considered excellent materials for manufacturing products requiring extremely high mechanical properties for various applications including thin medical devices, such as biodegradable intravascular stents. It is also proven that the addition of Ag can guarantee an appropriate degradation while implanted in human body without affecting its bioactive properties. In order to develop an optimized manufacturing process for thin stents, the effect of Ag on the recrystallization behavior of TWIP steels needs to be elucidated. This is of major importance since manufacturing stents involves several intermediate recrystallization annealing treatments. In this work, the recrystallization mechanism of two Fe-Mn-C steels with and without Ag was thoroughly investigated by microstructural and mechanical analyses. It was observed that Ag promoted a finer microstructure with a different texture evolution, while the recrystallization kinetics resulted unaffected. The presence of Ag also reduced the effectiveness of the recrystallization treatment. This behavior was attributed to the presence of Ag-rich second phase particles, precipitation of carbides and to the preferential development of grains possessing a {111} orientation upon thermal treatment. The prominence of {111} grains can also give rise to premature twinning, explaining the role of Ag in reducing the ductility of TWIP steels already observed in other works. Furthermore, *in vitro* biological performances were unaffected by Ag. These findings could allow the design of efficient treatments for supporting the transformation of Fe-Mn-C steels alloyed with Ag into commercial products.

1. Introduction

Biomaterials for medical devices have saved or improved the life and its quality for millions of patients around the globe in the last decades. Biodegradable metals are a new class of metallic biomaterials that open new horizons for revolutionising advanced surgical treatments. For example, metallic biodegradable stents, temporary devices used to restore blood flow in obstructed vessels [1], are expected to dissolve into the body after 1–2 years from their implantation [2]. The first commercial vascular device was based on a Mg – rare earth element alloy, and was approved by the European regulatory agency in 2016 [3]. While this stent meets the requirements in terms of resorption in the human body and biological performances [4–6], its low mechanical properties limit device miniaturization and, as a consequence, its deliverability in smaller vessels [7,8]. To fill this gap and satisfy cerebral and pediatrics needs, the development of biodegradable alloys suitable to produce reduced strut thickness devices is urgently required.

Twinning-induced plasticity (TWIP) steels, mainly composed of Fe, Mn and C, represent candidates of choice to manufacture small stents. This alloy family possesses equivalent mechanical properties to Co-Cr alloys [9,10] and their high amount of Mn stabilizes austenite at room temperature [11], whose paramagnetic behavior favors

Peer review under responsibility of KeAi Communications Co., Ltd.
* Corresponding author.
E-mail address: diego.mantovani@gmn.ulaval.ca (D. Mantovani).
URL: http://ww.lbb.ulaval.ca (D. Mantovani).

https://doi.org/10.1016/j.bioactmat.2021.10.020
Received 20 October 2020; Received in revised form 15 April 2021; Accepted 18 October 2021
Available online 21 October 2021

post-implantation imaging [2]. At the same time, the degradation behavior of such steels is inappropriate in the long-term: several *in vitro* and *in vivo* studies found that a stable corrosion layer is formed during the first weeks of implantation, reducing corrosion rate [12–14]. The addition of Ag to TWIP steels showed the ability to accelerate the short-term corrosion of these alloys [15–17]. In addition, the choice of Ag is of great interest because of its antibacterial properties [18]; furthermore, it was proven that Ag does not reduce the mechanical properties of TWIP steels below acceptable values [19,20].

In order for TWIP steels to be used as biodegradable stents, the material must be processed in the final shape through high plastic deformation processes, most commonly hot extrusion followed by cold drawing [21]. A recrystallization annealing treatment is normally performed after each drawing pass to restore the mechanical properties of the material. Successively, laser cutting and acid pickling are performed to obtain a stent from the drawn tubes and, after most of these steps, a further recrystallization annealing is again conducted. Finally, electropolishing is carried out to give the stent the final surface roughness, adequate for implantation.

It can thus be seen that recrystallization annealing treatments represent a critical step in manufacturing biodegradable stents. In fact, recrystallization of TWIP steels is in general a fast process, leading to nucleation of twin-free grains that grow over time [11,22]. When elements capable of forming second phases are added to TWIP steels, they impact significantly their recrystallization mechanism, as demonstrated in the case of V or Pd [23,24]. Ag is also known to form second phases in TWIP steels [19,20], potentially affecting their recrystallization behavior. Such a potential effect, unknown at the actual state of the art, can strongly influence the processing parameters that are the most suitable for the production of small devices such as stents, including the need to adjust thermal treatments to ensure that the final product can be manufactured with the appropriate dimensional, microstructural and mechanical specifications. This work aims at understanding the impact of Ag on the recrystallization mechanism of a Fe-Mn-C TWIP steel, and to assess its implications on plastic deformation processes. The recrystallization behavior of two TWIP steels (one with and one without Ag) as a function of treatment temperature and time was assessed in terms of microhardness, microstructure and texture evolution. Furthermore, the effect of Ag on both cytocompatibility and hemocompatibility was studied in order to validate the biological potential of such alloys for vascular implants. The steels produced during the work were cast and cold rolled in order to simulate the production process of a stent with a simplified laboratory setup.

2. Materials and methods

2.1. Material preparation and processing

Two alloys, with nominal composition Fe-16Mn-0.7C (wt. %) and Fe-16Mn-0.7C-0.4Ag (wt. %) and named 0Ag and 0.4Ag, respectively, were produced and processed as described elsewhere [20]. After hot rolling the cast billets at 800 °C from a size of 12.5 mm down to plates of thickness 1.33 mm, thin sheets of both alloys were cold rolled imposing a 25% thickness reduction. This condition constituted the starting point for recrystallization annealing treatments.

Coupons of 10 mm × 10 mm x 1 mm were cut from cold rolled sheets in order to understand the recrystallization behavior as a function of the annealing temperature. Each coupon underwent a thermal treatment of 10 min in a resistance furnace operating in air (Lenton AWF 13/25, UK) and a subsequent water quenching to freeze the microstructure and precisely stop the treatment time. The selected temperatures varied from 500 °C to 950 °C with a step of 50 °C.

In order to evaluate the effect of the annealing time on the recrystallization behavior, other coupons of both alloys underwent thermal treatments at 700, 800 and 900 °C for 2, 5, 10, 15, 20, 30, 60 min, and subsequently water quenched.

2.2. Microstructural characterization

Before performing any analysis, all samples were mechanically polished with SiC abrasive papers up to 600 grit. Successively, fine polishing was performed with diamond paste of 3 μm and 1 μm. Final polishing was carried out with a 0.05 μm colloidal alumina suspension.

The recrystallization curve was built by means of at least 5 Vickers microhardness indentations, using a load of 4.9 N and a dwell time of 15 s on each sample (FM-810, Future-Tech Corp., Japan). The phases present in each alloy as a function of the recrystallization treatment were evaluated by X-ray diffraction (XRD, SmartLab, Rigaku, Japan). XRD analyses were performed at a scanning rate of 3°/min in the range of 20–100° (stepsize 0.020°), using Cu K_α radiation ($\lambda = 1.5406$ Å) at 40 kV and 40 mA with a Bragg-Brentano geometry. Peak identification was performed using the SmartLab Studio II software (Rigaku, Japan).

The microstructure of both alloys as a function of the thermal treatment was evaluated by scanning electron microscopy (SEM), using a field emission gun SEM (FEG-SEM, Sigma 500, Zeiss, Germany). Prior to observation, samples were chemically etched with the Picral reagent (4 g picric acid in 100 ml ethanol). The composition of second phases was evaluated by energy dispersion x-ray spectroscopy (EDS, Ultim Max, Oxford Instruments, UK). Their average size and fraction were quantified by means of the ImageJ software (National Institute of Health, USA) using a scan area of 2.1 mm^2 for all conditions. Only particles with an area of at least 1 μm^2 were included in the analysis. Electron backscattered diffraction (EBSD, C-Nano, Oxford Instruments, UK) was performed to assess the grain orientations, the evolution of texture components, recrystallized fraction and Schmid factors distribution inside the materials, before and after annealing at 800 °C for 10 min. A scan area of 120 × 80 μm was used, resulting in at least 300 grains analyzed for each sample. The threshold for a grain to be counted as such was set at 10 pixels, as recommended by the ISO 13067:20 standard. For EBSD analyses, in addition to the previously described polishing procedure, samples were polished with colloidal silica (0.05 μm) for 20 min and rinsed with deionized water for 10 min in order to avoid any surface contamination. The obtained data were analyzed with the Channel5 software (Oxford Instruments, UK). The indexing rate for the analyzed conditions was of at least 82% for the deformed samples and of at least 97% for the annealed samples.

Finally, in order to validate the phases that precipitated during the various thermal treatments, a thermodynamic simulation of the amount of phases present at equilibrium as a function of temperature was carried out using the Thermocalc software using the TCFE9 database. Scheil non-equilibrium calculations were also carried out to establish the phases that could form in the alloy during solidification. However, since Ag is not available in the database, the calculation was carried out only for the 0Ag alloy.

2.3. Biological characterization

In order to verify that the presence of Ag did not alter the biological performances of the 0Ag alloy, both cytocompatibility and hemocompatibility tests were carried out on the material after annealing at 800 °C using 316L stainless steel as negative control. 5 replicates were used for cytocompatibility assays at each timepoint, while 3 replicates were used for clotting time and hemolysis tests. Before all biological experiments, samples were sterilized by UV irradiation. Briefly, each side of the samples underwent 2 15-min cycles of UV irradiation. Samples were stored in a sterile 24 multi-well plate until use.

2.3.1. Cytocompatibility assays

Cell culture. Human umbilical vein endothelial cells (HUVECs) and human umbilical artery smooth muscle cells (HUASMCs) were used in this study. Cells were isolated from human umbilical cord samples obtained from normal term pregnancies. Written informed consent was obtained from all mother donors according to the Declaration of

Helsinki. All experiments were performed in compliance with the Canadian Tri-Council Policy Statement: Ethical Conduct for Research Involving Humans and institutional CHU de Quebec - Laval University guidelines. The protocol was approved by the Ethics Committee of the CHU de Quebec Research Centre (CER #S11-03-168). Cells were isolated as described elsewhere [25]. Both the isolated HUVECs and HUASMCs were maintained at 37 °C in a saturated atmosphere at 5% CO_2 in M199 culture medium (Gibco, Invitrogen Corporation, Burlington, ON, Canada) addition with the supplements presented in Table 1. When 85%–90% of confluence was reached, cells were then enzymatically detached from the plate (0.05% trypsin, Gibco, Invitrogen Corporation, Burlington, ON, Canada) and then reseeded at a ratio of 1:3 or used for experiments. For the experiment here reported, HUVECs have been used at passage 5 and HUASMC at passage 7.

Indirect viability assays. The indirect cytotoxicity test was performed following the ISO 10993–5:2009 procedure. SS316L has been used as a reference material. Briefly, 1 cm^2 samples were immersed in 660 μl of M199 culture medium, supplemented with 1% P/S for 1, 3 and 7 days and incubated at 37 °C in a saturated atmosphere at 5% CO_2. At each time point, medium has been collected from samples and subsequently used for the viability test. Viability tests have been performed using different concentration of the extracted media: respectively 100%, 10% and 1% dilutions. Before putting them in contact with cells, extracted media have been supplemented with the supplements presented in Table 1 (with the exception of P/S). Briefly, HUVECs and HUASMCs were seeded in the well of 96 multi-well plates at a density of 20000 cells/cm^2 and incubated at 37 °C, 5% CO_2 for 24 h in 100 μl/well of the respective complete M199. The day after, medium was removed and 100 μl of the 100, 10 and 1% extracts dilutions were added to the well containing the HUVECs and HUASMCs and incubated for 24 h. The extracts were then removed and 100 μL of 1% solution of resazurin sodium salt in complete M199 medium were added to the cells and incubated for 4 h at 37 °C and 5% CO_2. After the incubation, the solutions containing the now reduced resorufin product were collected and fluorescence intensity at a 545 nm_{ex}/590 nm_{em} wavelength was measured with a SpectraMax i3x Multi-Mode Plate Reader (Molecular Devices, San Jose, California, USA). Fluorescence intensity is proportional to cell viability.

2.3.2. Hemocompatibility assays

For assessing the hemocompatibility, both clotting time and hemolysis tests were carried out using the same materials employed for cytocompatibility assays.

Hemolysis. Whole human blood from a healthy donor has been collected in citrate-containing blood collection tubes. Each sample has been placed in a 15 mL tube and 10 mL of sterile PBS 1X have been added in each tube. PBS 1X has been used as a negative control and deionized H_2O as positive control. Samples and controls have been incubated at 37 °C for 30 min. In the meantime, the collected blood has been diluted in PBS 1X to a final ratio of 4:5 (4 parts of citrated blood and 5 parts of PBS 1X). After the incubation, 200 μL of diluted blood were added in each tube and carefully mixed by inverting each tube. After that, samples and controls were incubated at 37 °C for 1 h. All tubes have been carefully mixed by inversion after 30 min of incubation. At the end of the incubation, the tubes containing the samples and the controls underwent a centrifugation step at 800 g for 5 min. The supernatant was collected and 100 μL aliquots were placed in a 96-well plate. The absorbance (OD) at a wavelength of 540 nm has been recorded. Hemolysis has been calculated as follows:

$$\textbf{\textit{Hemolysis}} = \frac{OD\ samples - OD\ CTRL\ Pos}{OD\ CTRL\ Pos - OD\ CTRL\ Neg}\ x\ 100$$

Clotting time. Whole human blood has been collected in citrate-containing blood collection tubes. Sterile samples have been placed in the wells of 24-well multi plates for the test. Briefly, 100 μl of citrated blood have been placed on the surfaces of the different samples (culture-treated plastic has been used as a control). Immediately after, 20 μl of calcium chloride ($CaCl_2$) has been added to the blood in order to activate the coagulation cascade ($CaCl_2$ inactivates the citrate). Samples have been then incubated at 37 °C for the selected time points (0, 15, 30, 45 and 60 min). At each time point, 2 ml of deionized water have been added to each sample in order to lysate the erythrocytes not entrapped in a blood clot. The aqueous solutions containing the free hemoglobin have then been transferred to a 96 well plates. Absorbance at a wavelength of 540 nm have been recorded using a Spectra Max i3x (Molecular Devices). Absorbance is proportional to the amount of free hemoglobin. Therefore, the higher the absorbance, the higher the amount of hemoglobin, the higher the hemocompatibility.

Table 1
list of supplements for cell culture media. * Gibco, Invitrogen Corporation, Burlington, ON, Canada; ** Life Sciences, Grand Island, NY, USA; *** Sigma Aldrich, Oakville, ON, Canada; ° Santa Cruz Biotechnology, Inc, Dallas, TX, USA.

Supplement	HUVECs Medium	HUASMCs Medium
Fetal Bovine Serum (FBS) *	5%	5%
Penicillin/Streptomycin (P/S) *	1%	1%
Fibroblast Growth Factor (FGF) **	2 ng/ml	2 ng/ml
Endothelial Growth Factor (EGF) **	1 ng/ml	0.5 ng/ml
Ascorbic Acid ***	1 μg/ml	-
Hydrocortisone ***	1 μg/ml	-
Human Insulin °	-	5 μg/mL

2.4. Statistical analyses

All data are reported with standard deviation errors. In Fig. 1, the error bars represent the uppermost and lowermost deviations from the average of each point. In order to estimate the statistical significance of differences in Vickers microhardness values, one-way ANOVA tests with Tukey's post-hoc analysis was carried out using the Minitab18 software (Minitab Inc., USA). The differences were considered statistically significant if $p < 0.05$ at least.

For biological tests, the data shown are means ± standard deviation (SD). Statistical significance has been calculated using ANOVA non-parametric Kruskal-Wallis method with Dunn post-test through the software InStat ™. Values of $p < 0.05$ or less have been considered significant.

3. Results

3.1. Vickers microhardness

The results obtained from Vickers microhardness tests are reported in Fig. 1. The microhardness curve as a function of temperature for thermal treatments of 10 min (Fig. 1a) showed that no sharp drop of hardness occurred for temperatures below 600 °C, suggesting that no recrystallization takes place in this temperature range. Recovery occurred at 600 °C, as inferable from the drop in hardness, while full recrystallization appeared to be achieved for temperatures exceeding 650 °C, as visible from the lower hardness plateau. Fig. 1a also suggests that the two investigated alloys feature a substantially similar recrystallization behaviour. The 0.4Ag alloy showed higher microhardness values for temperatures above 600 °C. This could be due to higher misfit strains stored inside the material caused by the precipitation of carbides at grain boundary, as will be shown in sections 3.2 and 3.4.

Looking at the evolution of microhardness as a function of time (fig. 1b and c), it could be seen that the treatment time had no effect in changing the microhardness of both alloys. This was attributed to the very fast recrystallization kinetics of TWIP steels, as already observed by other authors [26,27]. The only deviation from this behavior consisted in a marked increase in microhardness for the 0.4Ag alloy annealed at 900 °C for at least 30 min.

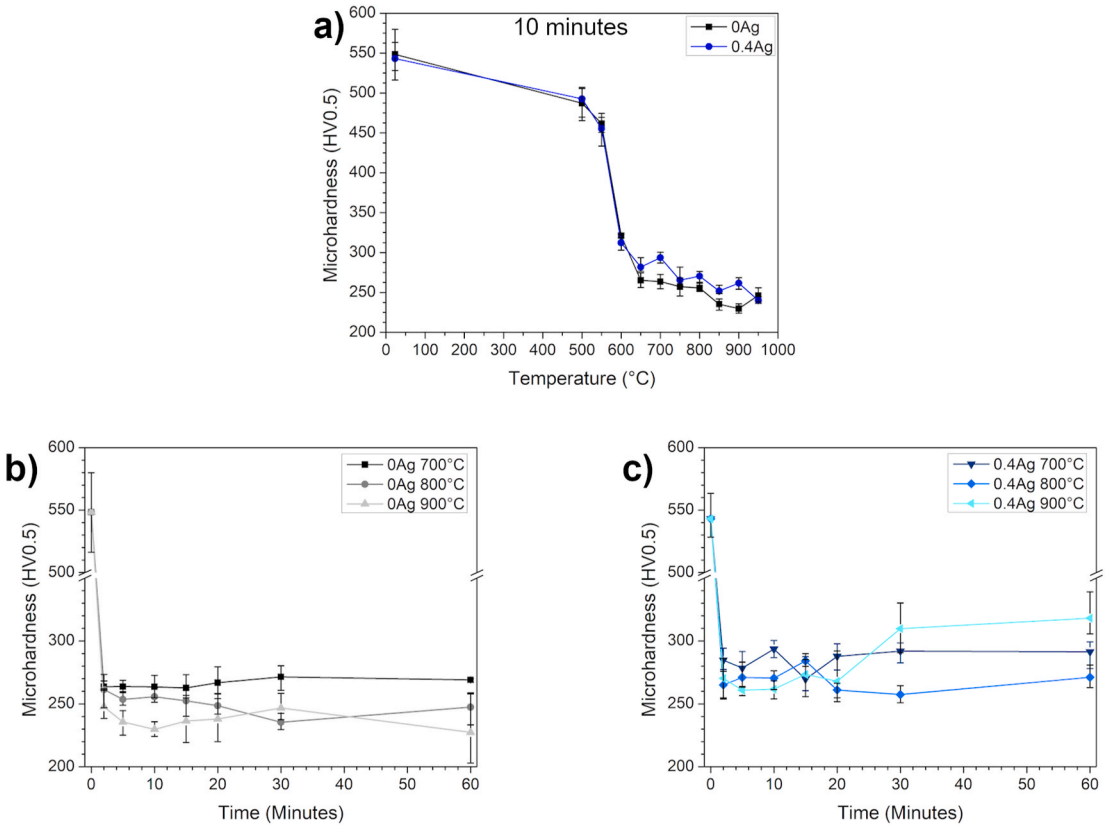

Fig. 1. Evolution of Vickers microhardness as a function of the thermal treatment parameters for the 0Ag and 0.4Ag alloys: a) 0Ag and 0.4Ag after 10 min as a function of temperature; b) 0Ag at 700 °C, 800 °C and 900 °C as a function of time; c) 0.4Ag at 700 °C, 800 °C and 900 °C as a function of time.

3.1.1. Scanning electron microscopy

Fig. 2 reports the microstructures of both alloys before and after annealing treatments at 500 °C, 600 °C and 800 °C for 10 min. In both cases, after treatment at 500 °C, second phases precipitated at grain boundaries without observing nucleation of new grains. Cold rolled grains started to be replaced at 600 °C, while precipitates were still present in both alloys; replacement appeared to be completed at 800 °C. At temperatures of 800 °C and above, it appeared that such second phases disappeared for the 0Ag alloy, while they were still present in the 0.4Ag alloy.

The nature of the second phase particles of the 0.4Ag alloy in both the as deformed state (CR25) and after a 500 °C treatment (10 min) was studied by EDS element mapping (Fig. 3). In the CR25 state (fig. 3a–e) just one type of second phase was detected: Ag-rich particles containing traces of Fe and Mn.

After the 0.4Ag alloy underwent the thermal treatment at 500 °C (fig.

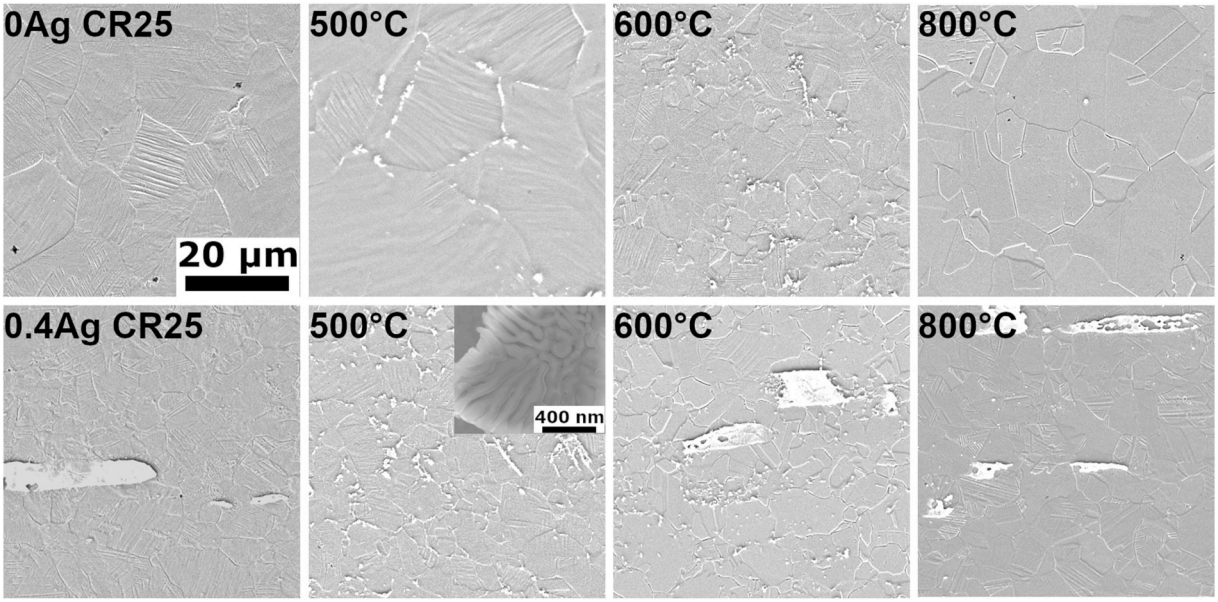

Fig. 2. SEM micrographs detailing the microstructural evolution of the studied alloys as a function of the recrystallization temperature after a 10-min treatment.

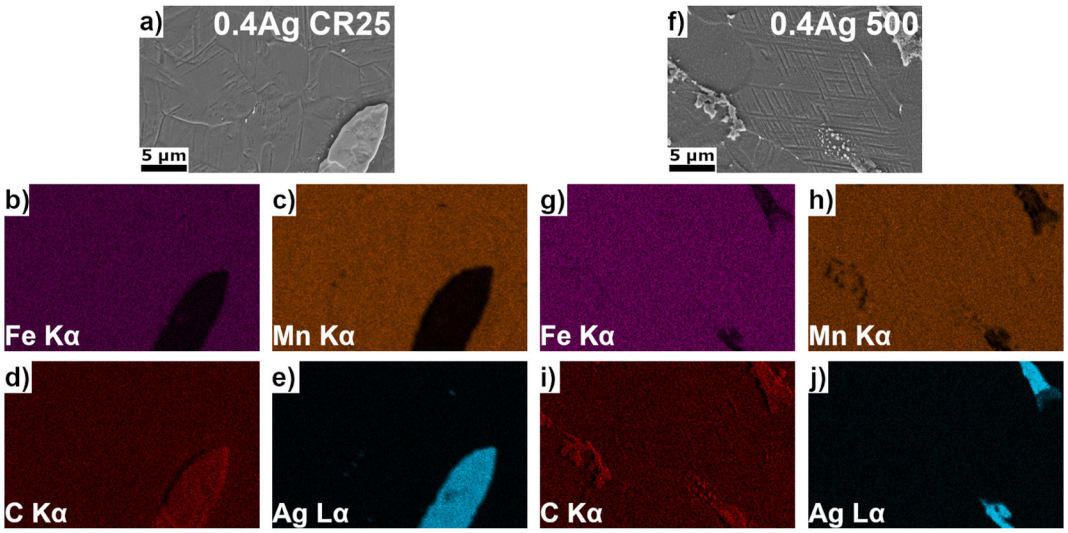

Fig. 3. EDS elemental mapping of 0.4Ag alloy in the unrecrystallized state, when a-e) cold rolled (**CR25**) and f-j) treated at 500 °C (**500**).

3f–j), two families of second phase particles were observed, also visible in the microstructure of Fig. 2, where Ag-rich particles and precipitates appeared segregated at grain boundaries. The Ag-rich particles had a similar composition to that observed prior to thermal treatments (fig. 3a–e). The precipitates at grain boundaries appeared to be depleted in Mn and Ag, while they were rich in Fe and C: this could indicate the precipitation of iron carbides at low temperatures, which was not observed for treatments above 900 °C.

The second phase particles in both alloys were quantified as a function of treatment temperature (Fig. 4). Portions of the images used for these calculations are reported in Fig. S1. For the 0.4Ag alloy, particles showing a size between 1 and 15 μm^2 were identified as carbides, while particles with an area above 15 μm^2 were identified as Ag-rich particles based on EDS observation (Fig. 3). The average carbide size (Fig. 4a) remained constant for both alloys independently from the treatment temperature. However, the area fraction was reduced by increasing the temperature: for the 0Ag alloy, pre-annealing fractions were re-established after a treatment at 800 °C, while this happened at 900 °C for the 0.4Ag alloy. In addition, the area fraction occupied by carbides was lower for the 0Ag alloy at all treatment temperatures.

The average size and area fraction of the Ag-rich particles (Fig. 4b) remained constant at all treatment temperatures, and it was comparable to that prior to any annealing treatment. Their size was very inhomogeneous, ranging from 15 to 276 μm^2. Differences in area fraction below 0.5% were detected due to the inhomogeneous distribution of such second phases (Fig. S1).

3.2. X-ray diffraction

The measured spectra from XRD analyses as a function of the treatment temperature for both alloys can be found in Fig. 5. It could be seen that the only detected phase for the 0Ag alloys was austenite (γ), independently from the applied thermal treatment (Fig. 5a). In addition, when the alloy containing Ag was considered (fig. 5b), a weak peak associated with the (111) plane of the face-centered cubic Ag phase also appeared in some conditions, depending on the local quantity of the phase. The Ag phase could be associated to the Ag-rich particles visible in Figs. 2 and 3. No peaks associated to ε-martensite were detected, contrarily to a previous work [20], where ε-martensite was detected in the cold rolled condition. This could be due to reversion of martensite to austenite during heating of the alloy.

3.3. Thermodynamic modelling

The phases formed in the 0Ag alloy as a function of temperature at equilibrium and during solidification are plotted in Fig. 6. From calculations at equilibrium (Fig. 6a), it can be observed that already starting from 745 °C, Fe_3C-type carbides (cementite) that then evolve into $M_{23}C_6$ at lower temperature are formed. Under strict equilibrium conditions, γ-Fe would progressively transform almost completely into α-Fe. This is apparently inconsistent with XRD and microstructural analyses indicating γ-austenite as the main matrix constituent. However, it can be considered that the investigated samples were analyzed after annealing

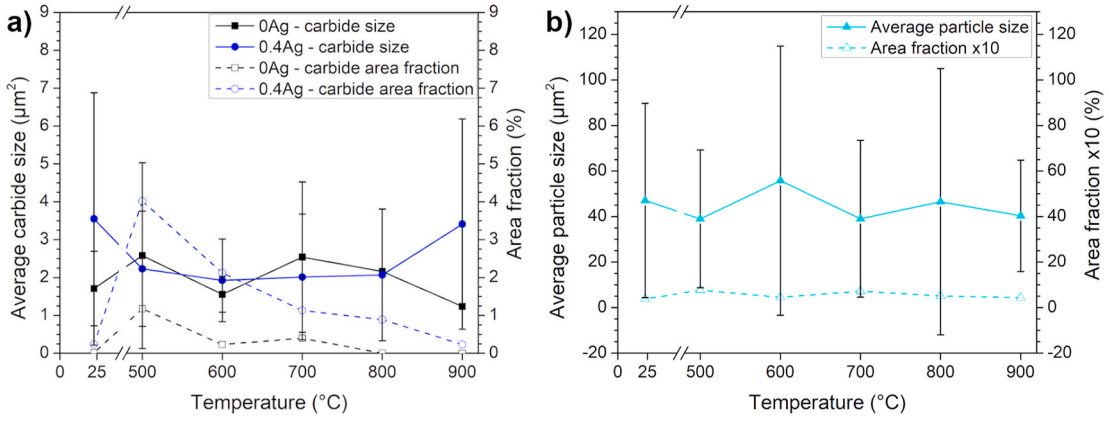

Fig. 4. Second phase particle size from ImageJ analyses: a) average carbide size and area fraction; b) average size and area fraction of the Ag-rich particles.

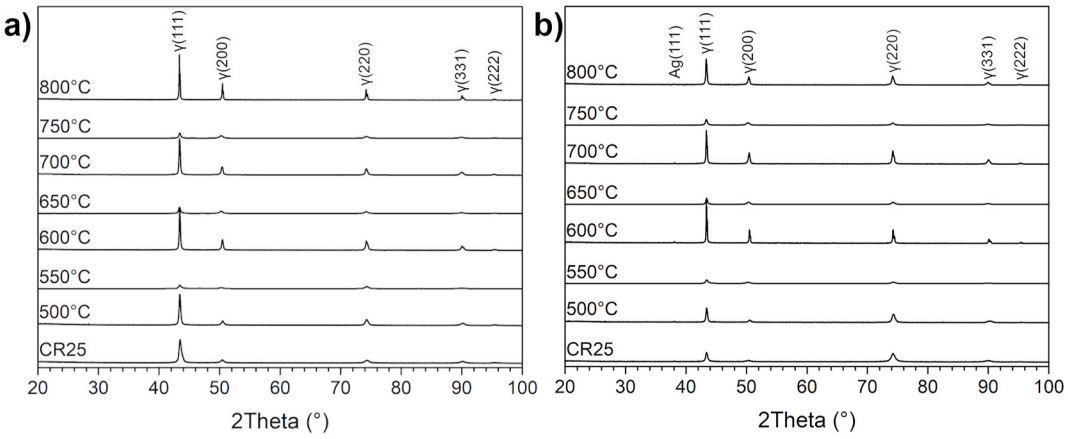

Fig. 5. XRD spectra of a) 0Ag and b) 0.4Ag alloys after different recrystallization treatments for 10 min.

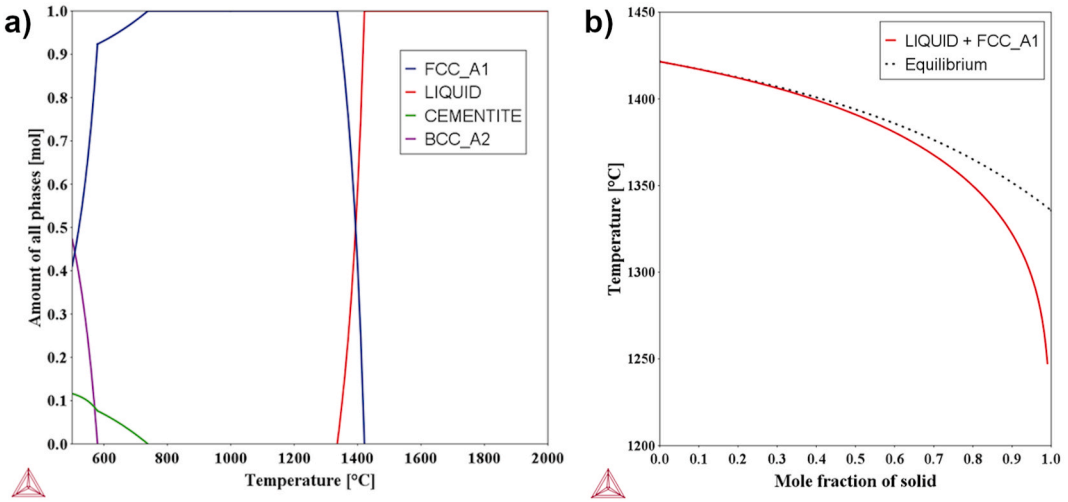

Fig. 6. Thermodynamic simulation of the phases formation as a function of temperature for Fe16Mn0·7C alloy (0Ag sample). a) Equilibrium calculation; b) Scheil-Gulliver non-equilibrium calculation.

at a fixed temperature and quenching. The rapid cooling tends to suppress the low-temperature transformation, preserving larger amounts of the structure created during the annealing holding period. Furthermore, the γ-Fe to α-Fe transformation in high Mn steels is believed to be quite sluggish due to the action of Mn and C as γ-stabilizers [11]. The Thermo-Calc simulation additionally allows to confirm that the tiny precipitates found at austenite grain boundaries can supposedly be carbides, either Fe_3C or more generally of $M_{23}C_6$ type.

From Scheil calculations, in agreement with the equilibrium calculation, the Liquid + FCC biphasic field appears at 1421 °C. Considering the Scheil plot (Fig. 6b), FCC is the only phase obtained from the solidification of the liquid phase for the Fe16Mn0·7C alloy and it ends at about 1250 °C. In the phase fraction vs T equilibrium plot the liquid phase is still present a t 1350 °C. From Scheil plot the cementite formation is not expected. The formation of the tiny precipitates of cementite can be attributed to the longer annealing applied at different temperatures. In this case, calculating the equilibrium for Fe16Mn0·7C at 600 °C, both FCC (0.94 vol fraction) and cementite (0.006 vol fraction) appear as stable phases.

3.4. Electron backscattered diffraction

Fig. 7 reports the orientation image maps (OIM) in the normal direction, inverse pole figure (IPF) in the normal direction and orientation distribution function (ODF) at $\varphi_2 = 45°$ for both alloys before and after the treatment at 800 °C for 10 min. The observed orientations were evenly spread in all cases: neither OIMs nor IPFs showed clear texturing of the material, as the maximum mean uniform deviation (MUD) of the strongest orientation components was always inferior to 2. When looking at the ODFs, the Brass {110}<112> component was present in both alloys prior to annealing, as commonly observed for TWIP steels [11, 22], and it was an indication of twinning during plastic deformation. The rotated Goss {110}<110> component was also detected for the 0Ag alloy, while an intermediate texture position between the Copper components and the γ fiber was detected for the 0.4Ag alloy.

After annealing, the ODFs highlight several texture components that developed during this process, replacing the Brass component observed after cold rolling. The two main texture components were the Cube {001}<110> and the F {111}<112> ones associated to the γ fiber, together with the Copper {112}<111> and Rotated Copper {112}<110> ones.

Fig. 8 reports image quality maps (IQ) in the band slope mode, allowing to qualitatively understand the amount of deformation stored inside each grain before and after annealing. Both alloys presented significant levels of deformation after cold rolling, with both mechanical twins and deformation bands present inside the grains. After annealing, the 0Ag alloy showed an almost deformation-free structure, contrarily to the 0.4Ag alloy. This can indicate that recrystallization of the material was hampered by the presence of Ag, as further confirmed by the analysis of the recrystallized fraction (Fig. S2). In addition, it was found

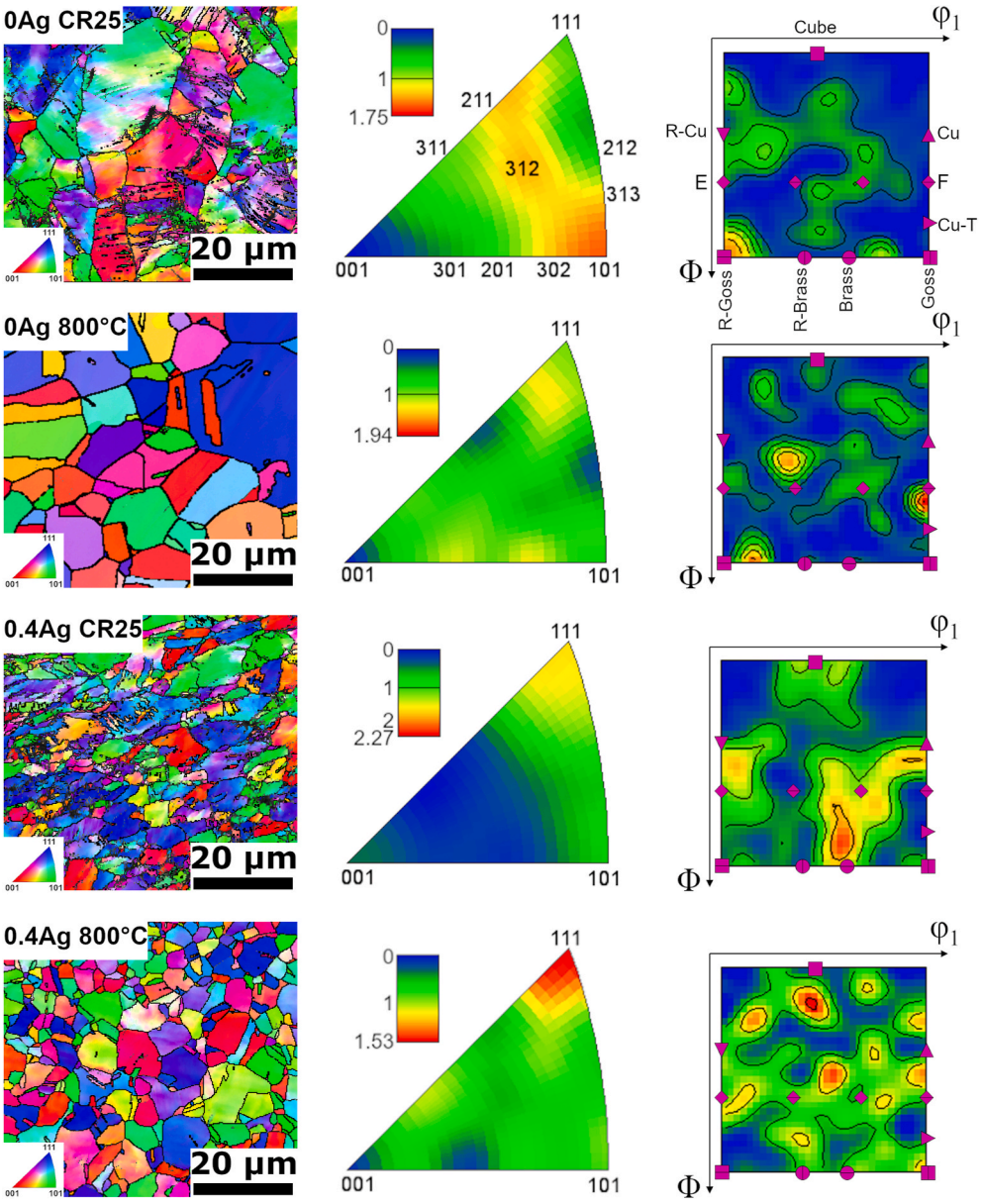

Fig. 7. EBSD maps of both alloys in both cold rolled (**CR25**) and treated (800 °C;10 min) (**800**) states. From left to right: orientation image maps (OIM), inverse pole figures (IPF) and orientation distribution functions (ODF) at $\varphi_2 = 45°$. The map of orientations in the IPFs is described in the top center figure. The relative intensity of each orientation is represented by the color scale, detailed in the histograms each IPF. The map of the ideal texture components for ODFs is detailed in the top right figure.

that the grain size distribution is concentrated to much lower values for the 0.4Ag alloy, as outlined in Fig. 9.

Fig. 10 reports the Schmid factors distribution in the analyzed regions for both alloys. This was not significantly affected by the recrystallization process for the 0Ag alloy. In addition to this, the vast majority of grains showed a Schmid factor above 0.4, indicating that no premature twinning occurred upon deformation of the recrystallized material [28]. For the 0.4Ag alloy, on the other hand, it could be seen that the annealing treatment reduced the number of grains having a Schmid factor lower than 0.4, while providing more grains with a Schmid factor higher than 0.4. Contrarily, the distribution of Schmid factor in the grains was broader than in the 0Ag alloy.

3.5. Biological tests

Fig. 11 reports the results obtained from both cytocompatibility and hemocompatibility tests of the Ag-free and Ag-containing alloy compared with the well known 316L stainless steel and the appropriate controls. The cytocompatibility towards both ECs (Fig. 11a) and SMCs at 1% eluate concentration (Fig. 11b) showed that Ag did not cause any reduction in viability with respect to the Ag-free counterpart. However, the relative viability of the studied TWIP steels was significantly reduced with respect to that of 316L SS towards ECs. On the contrary, no statistically significant difference was observed between the viability of all alloys towards SMCs. Similar results were observed with 10% and 100% eluate concentrations (Fig. S3).

Clotting time results (Fig. 11c) showed that both TWIP steels have a better hemocompatibility with respect to 316L SS at 30′, 45′ and 60’. In addition, both alloys showed comparable hemolysis to that of 316L SS (Fig. 11d), well below the 5% threshold outlined in the ASTM F756 standard as critical hemolysis value.

4. Discussion

It was observed that the addition of 0.4 wt %. of Ag influenced the microstructure of a Fe-16Mn-0.7C TWIP steel after recrystallization annealing. The microstructural evolution of the two alloys was found significantly different. Nevertheless, the overall recrystallization kinetics was globally unaffected since the microhardness evolution was very similar for both the alloys.

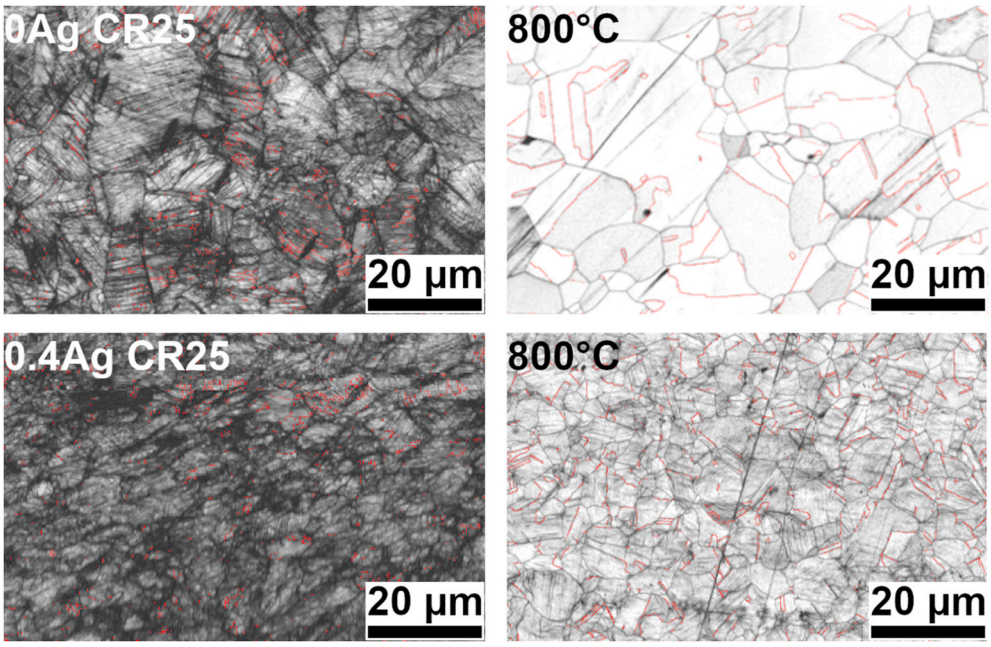

Fig. 8. Band slope image quality maps. Red lines inside the grains indicate twin boundaries; the other lines are deformation bands.

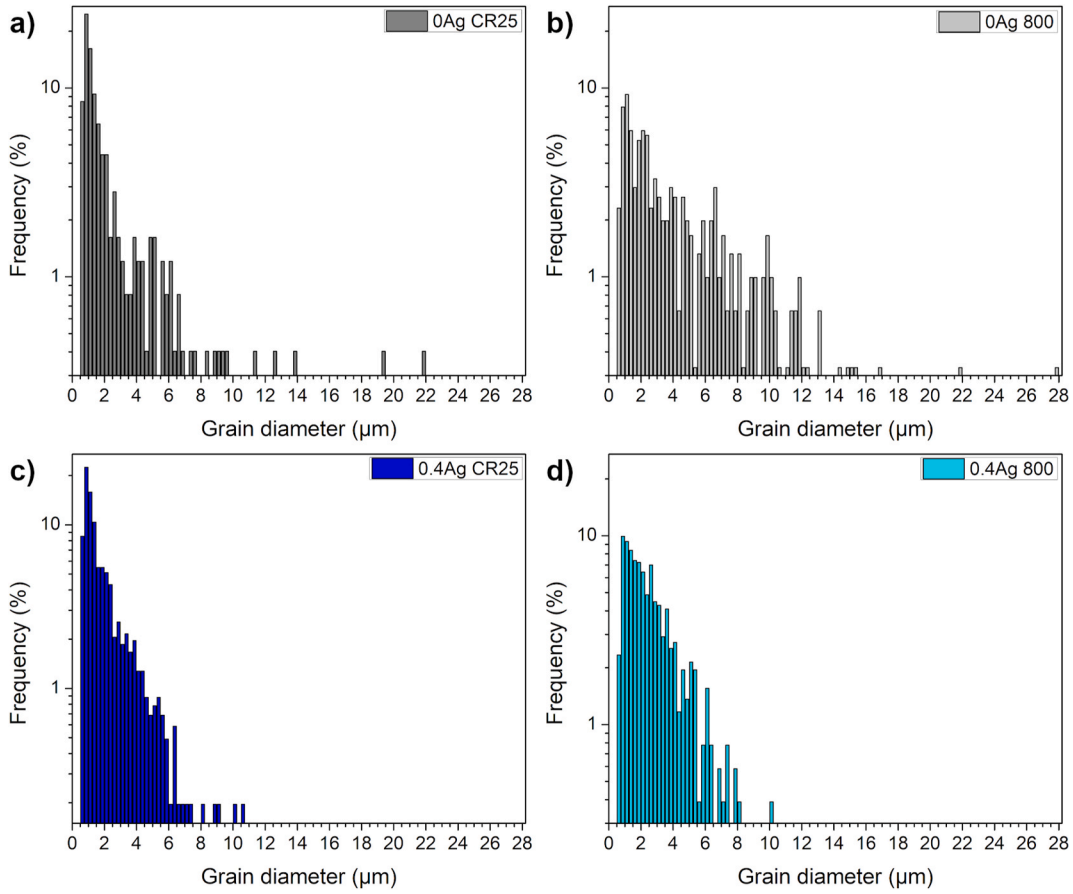

Fig. 9. Grain size distribution for the studied materials before (**CR25**) and after annealing at 800 °C for 10 min (**800**): a) 0Ag **CR25**; b) 0Ag **800**; c) 0.4Ag **CR25**; d) 0.4Ag **800**.

4.1. Recrystallization kinetics

The Vickers microhardness evolution (Fig. 1) was not affected by the presence of Ag. On the other hand, the plateau observed for treatment temperatures of at least 650 °C was at higher values for the 0.4Ag alloy. This finding contrasts with other works, which showed that the addition

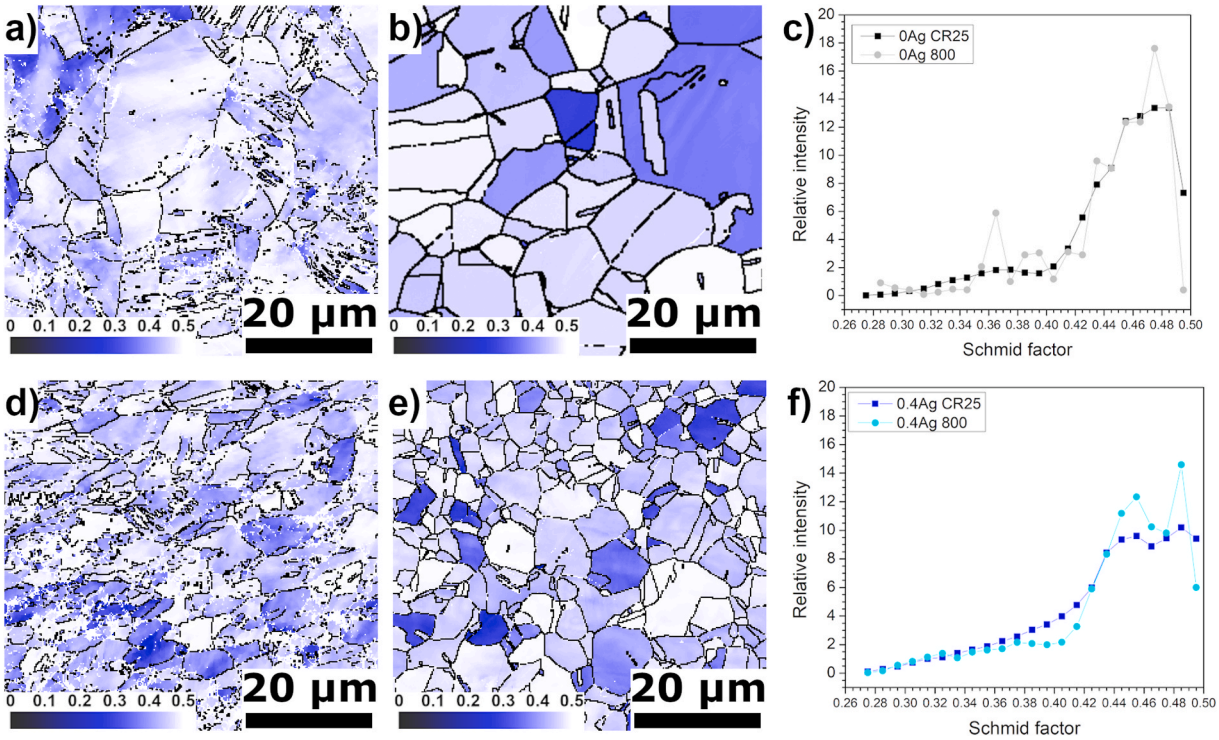

Fig. 10. Schmid factor data of both alloys in the cold rolled (**CR25**) and annealed (800 °C; 10 min) (**800**) states along the normal direction. Schmid factor map (0Ag **CR25**:a); **800**:b); 0.4Ag **CR25**:d); **800**:e)); comparison of Schmid factors intensities in CR25 and 800 states (0Ag:e), 0.4Ag:f)).

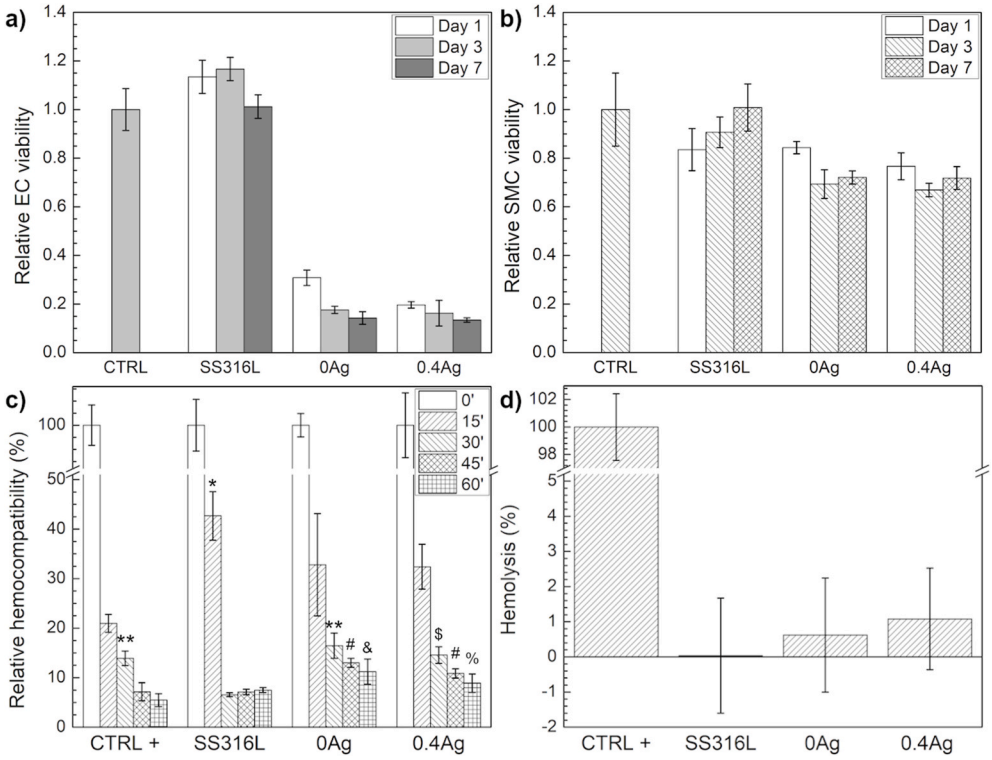

Fig. 11. Results from biological assessment of both 0Ag and 0.4Ag alloys compared to 316L stainless steel. a) relative viability towards endothelial cells (ECs) at 1% elution; b) relative viability towards smooth muscle cells (SMCs) at 1% elution; c) relative hemocompatibility from clotting time tests at 0, 15, 30, 45, 60 min; d) relative hemolysis. *p < 0.001 vs CTRL+ 15'; **p < 0.001 vs SS316L 30'; $ p < 0.01 vs SS316L 30'; #p < 0.001 vs CTRL+ and SS316L 45'; & p < 0.001 vs CTRL+ 60'; % p < 0.05 vs CTRL+ 60'.

of soluble elements (such as V and Pd) to a Fe-Mn-C matrix altered the recrystallization kinetics [23,24]. This different behavior can be explained by the high area fraction occupied by carbides in the presence of Ag, as visible from Fig. 4. The combined effect of carbides precipitating at grain boundary, together with the presence of Ag-rich particles, can obstruct grain nucleation and growth during thermal treatments, leading to higher deformations stored inside grains, as one can observe from both microhardness data (Fig. 1) and IQ maps (Fig. 8).

Another important phenomenon to be considered and analyzed was the evolution of grain size and twinning as a function of the annealing

temperature. It could be observed that the 0Ag alloy had a bigger grain size before and after annealing with respect to the Ag-containing alloy, as one could also notice from Fig. 9. This phenomenon could be reconducted to the presence of a higher area fraction of carbides and to the presence of Ag-rich particles in transgranular and intergranular positions, since they could hamper grain formation during thermal treatments. Such behavior was already observed by other authors in a Fe-Mn-C-Pd system [24], where Pd-rich particles precipitated inside grain boundaries and limited new grain nucleation and growth during annealing. This may also explain why the 0.4Ag alloy after annealing showed much higher internal deformations than the 0Ag alloy after the same treatment (Fig. 8).

An additional factor that played a role in reducing grain size of the 0.4Ag alloy after annealing was the precipitation of carbides observed at low temperatures (Figs. 2–4). These precipitates appeared rich in Fe and C, and their stoichiometry can be reconducted to carbides (either Fe_3C or $M_{23}C_6$), as determined by thermodynamic simulation (Fig. 6). It is known that precipitation of second phases at grain boundaries could obstacle the recrystallization process. Carbides appeared in higher amount for the 0.4Ag alloy heated between 500 and 800 °C. The precipitation of second phase particles was already observed by other authors in the case of prolonged thermal treatments on Fe-Mn-C alloys above 700 °C [26,29], limiting grain growth. In addition, a previous work on the same alloys [20] showed that nanoscale carbides were retained in the 0.4Ag alloy after annealing at 800 °C. On the contrary, the reason why such precipitates were preponderantly present when Ag was added is still unknown and requires further thermodynamic investigations to understand their formation kinetics and the role of Ag in favoring this phenomenon.

4.2. Texture evolution

It is clearly visible from Fig. 7 that the two alloys show some differences in preferential orientations and texture evolutions during annealing. The texture components in the 0Ag alloy changed during annealing at 800 °C according to the following evolution (CR25 → 800): (Rotated Goss + Brass) → (Rotated Goss + F). On the other hand, the 0.4Ag alloy showed the following texture evolution (CR25 → 800): (Brass + mixed Copper/γ fiber) → (Cube + Copper + γ fiber). In both cases, the Brass fiber was present in the deformed condition, which was typical of TWIP steels [11,22]. Moreover, as already observed by other authors, the texture evolution was relatively stable during the annealing process [26,30]. The presence of the Goss-type components is also typical of TWIP steels [30,31].

A noteworthy feature was the development of the γ-fiber during recrystallization in both alloys, which was already observed in an annealed state for a Fe-Mn-Al-Si TWIP steel [32]. On the contrary, the γ-fiber was also observed for heavily deformed TWIP steels by other authors [28,31,33]. In those cases, the development of the γ-fiber was related with the formation of shear bands at high levels of deformation, and they were considered preferential sites for recrystallization. In this work, no shear banding was detected in the cold rolled state (Figs. 2a and 3a), while only mechanical twinning was observed. At the same time, a preferential {111} orientation was developed after recrystallization (Fig. 7), which could explain the development of the γ-fiber during the recrystallization process.

Another phenomenon that could be related with the development of the γ-fiber during recrystallization was the retainment of grains possessing a Schmid factor below 0.4 (Figs. 8 and 10). This occurrence was preponderant in the 0.4Ag alloy: comparing Fig. 7 and Fig. 10d and e, it is clear that the grains with a lower Schmid factor were those possessing a {111} orientation, while the grains with a higher Schmid factor were those presenting a {101} orientation. The presence of {111} grains with a low Schmid factor was associated with an earlier onset of twinning during deformation by other authors [28]: this fact could definitively explain the role that Ag played in the ductility reduction of TWIP steels, as detected in previous works [19,20].

4.3. Impact of recrystallization annealing on processing

This work investigated the impact of Ag on recrystallization of a TWIP steel after cold rolling, which is a simplification of cold drawing, commonly used when manufacturing tubular precursors for stents [21]. Although the two processes differ in the distribution of applied forces generating plastic deformation [34], the impact of the second phases on recrystallization mechanism and microstructure are likely to affect the drawing processes required to thin the stent structure. It has been already reported that the presence of Ag impact the deformation mechanism of TWIP steels [20], and this has also be taken into account when designing thermal treatments. It was already demonstrated that tailoring recrystallization annealing treatments in TWIP steels can allow to finely tune grain size together with second phase size and shape, which in turn can alter processability and mechanical properties of final products [31,35,36]. Thermal treatments can also strongly impact texture evolution, which also affects the final microstructure and processability of TWIP steels into semi-finished products [31,37].

4.4. Impact of Ag on biological performances

The results outlined in section 3.6 showed that the studied TWIP steels have comparable biological performances to those of the commonly used 316L stainless steel. Only ECs and SMCs were used for assessing the effect of Ag on cytocompatibility since they compose the two innermost layers of an artery (*intima* and *media*) and they are the two vascular cell types that can get in contact with implanted stents. Proliferation of ECs is a wanted process since it implies acceptance of the stent by the organism, significantly reducing the risk of chronic inflammatory reactions. On the other hand, disproportionate SMC proliferation can lead to excessive neointimal proliferation, ultimately resulting in restenosis. From the results shown in Fig. 11a and b, it would appear that SMC proliferation would be the dominant process with respect to endothelialisation, possibly leading to chronic inflammatory reaction and ultimately to restenosis. These outcomes conform with findings reported by other authors [38–40]. Some factors should be kept in mind when discussing the outcomes from *in vitro* cytocompatibility assays. First, the environment into which such tests were carried out was a static one, while real conditions are dynamic since the stent is exposed to constant blood flow in the first 14–28 days of implantation. In addition, as one can observe from Fig. 11and S2, cell viability is clearly a function of the elution concentration. It could be hypothesized that, in a dynamic environment, the concentration of degradation products is lower than the most diluted eluates used in this work, leading to an increase in viability with respect to what was reported here. Finally, it should be noted that the contact time between cells and eluates was of 24 h, aiming at assessing acute effects. For studying chronic effects, *in vivo* tests should be carried out. The only report in an arterial environment for a Fe-Mn alloy [40] showed that endothelialisation was completed in 28 days, similarly to the case of pure Fe [41–43]. This suggests that chronic cytotoxicity of TWIP steels implants should not be a cause for concern.

Hemocompatibility tests showed that the studied TWIP steels have similar performances to those of 316L SS, which is comparable to what other authors observed [13]. In addition, the presence of Ag did not cause any decrease in hemocompatibility of the base alloy, similarly to what was reported by other authors on pure Fe [44,45]. These findings indicate that hemocompatibility of the studied TWIP steels should not be a cause for concern, which was also confirmed by *in vivo* studies on Fe-Mn alloys [40].

5. Conclusions

This work investigated the influence that Ag addition has on the

recrystallization behavior of a Fe-16Mn-0.7C TWIP steel. The presence of Ag resulted in a harder material after recrystallization, due to presence of carbides that limited grain nucleation and growth, leading to grains with higher local strain. Carbides and Ag-rich second phase particles were identified as the cause for the lower efficacy of the annealing treatment since they limited the nucleation and growth of twin-free grains. In addition to this, the presence of Ag stimulated the development of more {111} grains upon recrystallization, which presented a lower Schmid factor and were more prone to twinning upon plastic deformation. This observation could also explain why the addition of Ag provided a reduction in ductility to TWIP steels, which could be detrimental to the deployment of a stent in a diseased artery. Finally, it was found that Ag did not alter the biological performances of the studied steel. From the findings of this work, it is recommended to carry out annealing at temperatures above 800 °C for the Ag-free alloy and above 900 °C for the Ag-containing alloy to avoid precipitation of carbides and, as a consequence, prevent a significant reduction in ductility. Further works should focus on the actual process of tube drawing of TWIP steels, which was an unexplored topic in the literature at the time of submitting this article.

CRediT authorship contribution statement

Sergio Loffredo: Conceptualization, Methodology, Formal analysis, Investigation, Data curation, Writing – original draft, Visualization. **Sofia Gambaro:** Methodology, Software, Validation, Data curation, Writing – review & editing. **Francesco Copes:** Methodology, Formal analysis, Investigation, Data curation, Writing – review & editing. **Carlo Paternoster:** Conceptualization, Methodology, Writing – review & editing. **Nicolas Giguère:** Resources, Writing – review & editing. **Maurizio Vedani:** Methodology, Resources, Writing – review & editing, Supervision. **Diego Mantovani:** Resources, Writing – review & editing, Supervision, Funding acquisition.

Declaration of competing interest

Dear Dr Yufeng Zheng, We hereby declare that this manuscript has not been published and it is not under consideration for publication elsewhere. We have no conflicts of interest to disclose.

Acknowledgements

The authors would like to thank Marawan Abdelwahed, Ruben Beltrami, Maurizio Pardi and Ludovica Rovatti from Politecnico di Milano for assistance with XRD, SEM and EBSD analyses. The support of Jean-Nicolas Rousseau from Quebec Metallurgy Center for EBSD data analysis is also acknowledged. S. L. acknowledges funding from a Vanier Canada Graduate Scholarship (2017–2020). This work was partially supported by the Natural Science and Engineering Research Council of Canada (Discovery, Strategic, Collaborative Research and Development, and College-University-Industry Programs), the Quebec Ministry of Economy and Innovation, the Canadian Foundation for Innovation, and the FRQ-Santé through the support of the Research Center of the University Quebec Hospital, Regenerative Medicine Division.

Appendix A. Supplementary data

Supplementary data to this article can be found online at https://doi.org/10.1016/j.bioactmat.2021.10.020.

References

[1] J.A. Ormiston, P.W.S. Serruys, Bioabsorbable coronary stents, Circ. Cardiovasc. Interv. 2 (2009) 255–260, https://doi.org/10.1161/CIRCINTERVENTIONS.109.859173.

[2] Y.F. Zheng, X.N. Gu, F. Witte, Biodegradable metals, Mater. Sci. Eng. R Rep. 77 (2014) 1–34, https://doi.org/10.1016/j.mser.2014.01.001.

[3] H.M. Garcia-Garcia, M. Haude, K. Kuku, A. Hideo-Kajita, H. Ince, A. Abizaid, R. Tölg, P.A. Lemos, C. von Birgelen, E.H. Christiansen, W. Wijns, J. Escaned, J. Dijkstra, R. Waksman, In vivo serial invasive imaging of the second-generation drug-eluting absorbable metal scaffold (Magmaris — DREAMS 2G) in de novo coronary lesions: insights from the BIOSOLVE-II First-In-Man Trial, Int. J. Cardiol. 255 (2018) 22–28, https://doi.org/10.1016/j.ijcard.2017.12.053.

[4] M. Haude, H. Ince, A. Abizaid, R. Toelg, P.A. Lemos, C. von Birgelen, E. H. Christiansen, W. Wijns, F.-J. Neumann, C. Kaiser, E. Eeckhout, S.T. Lim, J. Escaned, H.M. Garcia-Garcia, R. Waksman, Safety and performance of the second-generation drug-eluting absorbable metal scaffold in patients with de-novo coronary artery lesions (BIOSOLVE-II): 6 month results of a prospective, multicentre, non-randomised, first-in-man trial, Lancet 387 (2016) 31–39, https://doi.org/10.1016/S0140-6736(15)00447-X.

[5] M. Haude, H. Ince, S. Kische, A. Abizaid, R. Tölg, P.A. Lemos, N.M. Van Mieghem, S. Verheye, C. Von Birgelen, E.H. Christiansen, W. Wijns, H.M. Garcia-Garcia, R. Waksman, Sustained safety and clinical performance of a drug-eluting absorbable metal scaffold up to 24 months: pooled outcomes of BIOSOLVE-II and BIOSOLVE-III, EuroIntervention 13 (2017) 432–439, https://doi.org/10.4244/EIJ-D-17-00254.

[6] S. Verheye, A. Wlodarczak, P. Montorsi, J. Bennett, J. Torzewski, M. Haude, M. Vrolix, T. Buck, A. Aminian, R.J. Van Der Schaaf, A. Amin, Nuruddin Michael, K.Y. Lee, Safety and performance of a resorbable magnesium scaffold under real-world conditions: 12-month outcomes of the first 400 patients enrolled in the BIOSOLVE-IV registry, EuroIntervention 15 (2019) e1383–e1386, https://doi.org/10.4244/EIJ-D-18-01058.

[7] N. Foin, R.D. Lee, R. Torii, J.L. Guitierrez-Chico, A. Mattesini, S. Nijjer, S. Sen, R. Petraco, J.E. Davies, C. Di Mario, M. Joner, R. Virmani, P. Wong, Impact of stent strut design in metallic stents and biodegradable scaffolds, Int. J. Cardiol. 177 (2014) 800–808, https://doi.org/10.1016/j.ijcard.2014.09.143.

[8] S.H. Im, Y. Jung, S.H. Kim, Current status and future direction of biodegradable metallic and polymeric vascular scaffolds for next-generation stents, Acta Biomater. 60 (2017) 3–22, https://doi.org/10.1016/j.actbio.2017.07.019.

[9] S. Loffredo, H. Hermawan, M. Vedani, D. Mantovani, Absorbable metals for cardiovascular applications, in: M. Niinomi (Ed.), Met. Biomed. Devices, second ed., Elsevier, 2019, pp. 523–543, https://doi.org/10.1016/B978-0-08-102666-3.00020-1.

[10] E. Mouzou, C. Paternoster, R. Tolouei, A. Purnama, P. Chevallier, D. Dubé, F. Prima, D. Mantovani, In vitro degradation behavior of Fe–20Mn–1.2C alloy in three different pseudo-physiological solutions, Mater. Sci. Eng. C 61 (2016) 564–573, https://doi.org/10.1016/j.msec.2015.12.092.

[11] O. Bouaziz, S. Allain, C.P. Scott, P. Cugy, D. Barbier, High manganese austenitic twinning induced plasticity steels: a review of the microstructure properties relationships, Curr. Opin. Solid State Mater. Sci. 15 (2011) 141–168, https://doi.org/10.1016/j.cossms.2011.04.002.

[12] T. Kraus, F. Moszner, S. Fischerauer, M. Fiedler, E. Martinelli, J. Eichler, F. Witte, E. Willbold, M. Schinhammer, M. Meischel, P.J. Uggowitzer, J.F. Löffler, A. Weinberg, Biodegradable Fe-based alloys for use in osteosynthesis: outcome of an in vivo study after 52 weeks, Acta Biomater. 10 (2014) 3346–3353, https://doi.org/10.1016/j.actbio.2014.04.007.

[13] C. Verhaegen, S. Lepropre, M. Octave, D. Brusa, L. Bertrand, C. Beauloye, P. J. Jacques, J. Kefer, S. Horman, Bioreactivity of stent material : in vitro impact of new twinning-induced plasticity steel on platelet activation, J. Biomaterials Nanobiotechnol. 10 (2019) 175–189, https://doi.org/10.4236/jbnb.2019.104010.

[14] E. Mouzou, C. Paternoster, R. Tolouei, P. Chevallier, C.A. Biffi, A. Tuissi, D. Mantovani, CO2-rich Atmosphere Strongly Affects the Degradation of Fe-21Mn-1C for Biodegradable Metallic Implants, 2016, https://doi.org/10.1016/j.matlet.2016.06.017.

[15] M. Wiesener, K. Peters, A. Taube, A. Keller, K.P. Hoyer, T. Niendorf, G. Grundmeier, Corrosion properties of bioresorbable FeMn-Ag alloys prepared by selective laser melting, Mater. Corros. 68 (2017) 1028–1036, https://doi.org/10.1002/maco.201709478.

[16] M. Caligari Conti, D. Aquilina, C. Paternoster, D. Vella, E. Sinagra, D. Mantovani, G. Cassar, P. Schembri Wismayer, J. Buhagiar, Influence of cold rolling on in vitro cytotoxicity and electrochemical behaviour of an Fe-Mn-C biodegradable alloy in physiological solutions, Heliyon 4 (2018), e00926, https://doi.org/10.1016/j.heliyon.2018.e00926.

[17] P. Sotoudehbagha, S. Sheibani, M. Khakbiz, S. Ebrahimi-Barough, H. Hermawan, Novel antibacterial biodegradable Fe-Mn-Ag alloys produced by mechanical alloying, Mater. Sci. Eng. C 88 (2018) 88–94, https://doi.org/10.1016/j.msec.2018.03.005.

[18] K. Mijnendonckx, N. Leys, J. Mahillon, S. Silver, R. Van Houdt, Antimicrobial silver: uses, toxicity and potential for resistance, Biometals 26 (2013) 609–621, https://doi.org/10.1007/s10534-013-9645-z.

[19] T. Niendorf, F. Brenne, P. Hoyer, D. Schwarze, M. Schaper, R. Grothe, M. Wiesener, G. Grundmeier, H.J. Maier, Processing of new materials by additive manufacturing: iron-based alloys containing silver for biomedical applications, Metall. Mater. Trans. 46 (2015) 2829–2833, https://doi.org/10.1007/s11661-015-2932-2.

[20] S. Loffredo, C. Paternoster, N. Giguère, G. Barucca, M. Vedani, D. Mantovani, The addition of silver affects the deformation mechanism of a twinning-induced plasticity steel: potential for thinner degradable stents, Acta Biomater. 98 (2019) 103–113, https://doi.org/10.1016/j.actbio.2019.04.030.

[21] H. Hermawan, D. Mantovani, Process of prototyping coronary stents from biodegradable Fe–Mn alloys, Acta Biomater. 9 (2013) 8585–8592, https://doi.org/10.1016/j.actbio.2013.04.027.

[22] B.C. De Cooman, Y. Estrin, S.K. Kim, Twinning-induced plasticity (TWIP) steels, Acta Mater. 142 (2018) 283–362, https://doi.org/10.1016/j.actamat.2017.06.046.

[23] H. Gwon, J.-K. Kim, S. Shin, L. Cho, B.C. De Cooman, The effect of vanadium micro-alloying on the microstructure and the tensile behavior of TWIP steel, Mater. Sci. Eng. 696 (2017) 416–428, https://doi.org/10.1016/j.msea.2017.04.083.
[24] M. Schinhammer, C.M. Pecnik, F. Rechberger, A.C. Hänzi, J.F. Löffler, P. J. Uggowitzer, Recrystallization behavior, microstructure evolution and mechanical properties of biodegradable Fe–Mn–C(–Pd) TWIP alloys, Acta Mater. 60 (2012) 2746–2756, https://doi.org/10.1016/j.actamat.2012.01.041.
[25] F. Copes, P. Chevallier, C. Loy, D. Pezzoli, F. Boccafoschi, D. Mantovani, Heparin-modified collagen gels for controlled release of pleiotrophin: potential for vascular applications, Front. Bioeng. Biotechnol. 7 (2019), https://doi.org/10.3389/fbioe.2019.00074.
[26] L. Bracke, K. Verbeken, L. Kestens, J. Penning, Microstructure and texture evolution during cold rolling and annealing of a high Mn TWIP steel, Acta Mater. 57 (2009) 1512–1524, https://doi.org/10.1016/j.actamat.2008.11.036.
[27] C. Scott, S. Allain, M.M. Faral, N. Guelton, The development of a new Fe-Mn-C austenitic steel for automotive applications, Rev. Métall. 103 (2006) 293–302, https://doi.org/10.1051/metal:2006142.
[28] S. Vercammen, B. Blanpain, B.C. De Cooman, P. Wollants, Cold rolling behaviour of an austenitic Fe-30Mn-3Al-3Si TWIP-steel: the importance of deformation twinning, Acta Mater. 52 (2004), https://doi.org/10.1016/j.actamat.2003.12.040, 2005–2012.
[29] Y. Ono, T. Tsuchiyama, S. Takaki, Microstructural change during isothermal aging in high manganese austenitic steels, Tetsu-To-Hagane 84 (1998) 309–314, https://doi.org/10.2355/tetsutohagane1955.84.4_309.
[30] D. Barbier, N. Gey, S. Allain, N. Bozzolo, M. Humbert, Analysis of the tensile behavior of a TWIP steel based on the texture and microstructure evolutions, Mater. Sci. Eng. 500 (2009) 196–206, https://doi.org/10.1016/j.msea.2008.09.031.
[31] C. Haase, L.A. Barrales-Mora, F. Roters, D.A. Molodov, G. Gottstein, Applying the texture analysis for optimizing thermomechanical treatment of high manganese twinning-induced plasticity steel, Acta Mater. 80 (2014) 327–340, https://doi.org/10.1016/j.actamat.2014.07.068.
[32] N.K. Tewary, S.K. Ghosh, S. Bera, D. Chakrabarti, S. Chatterjee, Influence of cold rolling on microstructure, texture and mechanical properties of low carbon high Mn TWIP steel, Mater. Sci. Eng. 615 (2014) 405–415, https://doi.org/10.1016/j.msea.2014.07.088.
[33] Y.F. Shen, Y.D. Wang, X.P. Liu, X. Sun, R. Lin Peng, S.Y. Zhang, L. Zuo, P.K. Liaw, Deformation mechanisms of a 20Mn TWIP steel investigated by in situ neutron diffraction and TEM, Acta Mater. 61 (2013) 6093–6106, https://doi.org/10.1016/j.actamat.2013.06.051.
[34] P. Poncin, J. Proft, Stent tubing: understanding the desired attributes, in: Med. Device Mater. Proc. Mater. Process. Med. Devices Conf. Mater. Park. OH, ASM Int., 2004, pp. 253–259.
[35] C. Haase, T. Ingendahl, O. Güvenç, M. Bambach, W. Bleck, D.A. Molodov, L. A. Barrales-Mora, On the applicability of recovery-annealed Twinning-Induced Plasticity steels: potential and limitations, Mater. Sci. Eng. 649 (2016) 74–84, https://doi.org/10.1016/j.msea.2015.09.096.
[36] D.B. Santos, A.A. Saleh, A.A. Gazder, A. Carman, D.M. Duarte, É.A.S. Ribeiro, B. M. Gonzalez, E.V. Pereloma, Effect of annealing on the microstructure and mechanical properties of cold rolled Fe-24Mn-3Al-2Si-1Ni-0.06C TWIP steel, Mater. Sci. Eng. 528 (2011) 3545–3555, https://doi.org/10.1016/j.msea.2011.01.052.
[37] J.K. Hwang, Correlation of strain path, texture, twinning, and mechanical properties in twinning-induced plasticity steel during wire drawing, Materials 13 (2020), https://doi.org/10.3390/ma13102250.
[38] E. Mouzou, Étude de la dégradation in-vitro d'alliages Fe-Mn-C pour des applications de stents cardiovasculaires, Université Laval, 2017.
[39] M. Schinhammer, I. Gerber, A.C. Hänzi, P.J. Uggowitzer, On the cytocompatibility of biodegradable Fe-based alloys, Mater. Sci. Eng. C 33 (2013) 782–789, https://doi.org/10.1016/j.msec.2012.11.002.
[40] A. Drynda, T. Hassel, F.W. Bach, M. Peuster, In vitro and in vivo corrosion properties of new iron-manganese alloys designed for cardiovascular applications, J. Biomed. Mater. Res. B Appl. Biomater. 103 (2015) 649–660, https://doi.org/10.1002/jbm.b.33234.
[41] M. Peuster, C. Hesse, T. Schloo, C. Fink, P. Beerbaum, C. von Schnakenburg, Long-term biocompatibility of a corrodible peripheral iron stent in the porcine descending aorta, Biomaterials 27 (2006) 4955–4962, https://doi.org/10.1016/j.biomaterials.2006.05.029.
[42] W.-J. Lin, D.-Y. Zhang, G. Zhang, H.-T. Sun, H.-P. Qi, L.-P. Chen, Z.-Q. Liu, R.-L. Gao, W. Zheng, Design and characterization of a novel biocorrodible iron-based drug-eluting coronary scaffold, Mater. Des. 91 (2016) 72–79, https://doi.org/10.1016/j.matdes.2015.11.045.
[43] W. Lin, L. Qin, H. Qi, D. Zhang, G. Zhang, R. Gao, H. Qiu, Y. Xia, P. Cao, X. Wang, W. Zheng, Long-term in vivo corrosion behavior, biocompatibility and bioresorption mechanism of a bioresorbable nitrided iron scaffold, Acta Biomater. 54 (2017) 454–468, https://doi.org/10.1016/j.actbio.2017.03.020.
[44] T. Huang, Y. Cheng, Y. Zheng, In vitro studies on silver implanted pure iron by metal vapor vacuum arc technique, Colloids Surf. B Biointerfaces 142 (2016) 20–29, https://doi.org/10.1016/j.colsurfb.2016.01.065.
[45] T. Huang, J. Cheng, D. Bian, Y. Zheng, Fe-Au and Fe-Ag composites as candidates for biodegradable stent materials, J. Biomed. Mater. Res. B Appl. Biomater. 104 (2016) 225–240, https://doi.org/10.1002/jbm.b.33389.